PCCP

PAPER

View Article Online
View Journal | View Issue

Check for updates

Cite this: *Phys. Chem. Chem. Phys.*, 2024, **26**, 12084

Received 1st February 2024,
Accepted 25th March 2024

DOI: 10.1039/d4cp00481g

rsc.li/pccp

Local symmetry-driven interfacial magnetization and electronic states in $(ZnO)_n/(w\text{-}FeO)_n$ superlattices†

Jia-Xin Gao,‡[a] Yi Sheng Ng, ‡[b] Hao Cheng,[c] Hui-Qiong Wang,*[ab] Tie-Yu Lü*[a] and Jin-Cheng Zheng *[ab]

Superlattices constructed with the wide-band-gap semiconductor ZnO and magnetic oxide FeO, both in the wurtzite structure, have been investigated using spin-polarized first-principles calculations. The structural, electronic and magnetic properties of the $(ZnO)_n/(w\text{-}FeO)_n$ superlattices were studied in great detail. Two different interfaces in the $(ZnO)_n/(w\text{-}FeO)_n$ superlattices were identified and they showed very different magnetic and electronic properties. Local symmetry-driven interfacial magnetization and electronic states can arise from different Fe/Zn distributions at different interfaces or spin ordering of Fe in the superlattice. The local symmetry-driven interfacial magnetization and electronic states, originating either from different Fe/Zn distribution across interfaces I and II, or by spin ordering of Fe in the superlattice, can be identified. It was also found that, in the case of the ferromagnetic phase, the electrons are more delocalized for the majority spin but strongly localized for the minority spin, which resulted in interesting spin-dependent transport properties. Our results will pave the way for designing novel spin-dependent electronic devices through the construction of superlattices from semiconductors and multiferroics.

1. Introduction

Due to broken periodicity, interfaces between distinct materials have manifested physical and chemical characteristics that are unique and absent in their bulk phase,[1] with two-dimensional electron gases (2DEGs) being the most notable examples.[2] Oxide interfaces have received particular attention in the past decades[3–6] due to the potential novel physics that they offer.[2,7,8] Heterostructures combining magnetic oxides and other non-magnetic oxides were studied for spin transfer in the search for suitable materials for spintronics, with both ferromagnetic and antiferromagnetic oxides being explored.[9]

A superlattice (SL) is a kind of material that contains a periodic structure of two or more layers of sublattices, which alternates in the growth direction and potentially offer unique features not found in the bulk phase of the constituent materials,[10] including superconductivity[11,12] and interface ferromagnetism.[13] Interfaces are everywhere in a SL, and the interfacial coupling that arises gives rise to many unique properties,[14,15] which can be controlled by varying the layer thickness, enabling the tuning of their properties.[16–19] Unsurprisingly, numerous applications have been discovered for SLs, *e.g.*, solar cells,[20,21] electronics,[22] and water splitting.[23,24]

ZnO is a wide-band-gap (∼3.4 eV) semiconductor with a wurtzite structure, where one zinc ion is tetrahedrally bonded to four oxygen ions. It possesses many desirable qualities, including a wide and direct band gap, low toxicity, ease of growth, and stability. Therefore, ZnO has received enormous attention in the past, and many potential applications have been investigated, ranging from optoelectronics,[25] photocatalysis,[26] power electronics,[27] and LEDs.[28] ZnO has also been used to form SLs along with other oxides, such as w-NiO, CuO, and w-MgO. The SLs formed have shown promising properties, for instance, ZnO/(w-NiO) and ZnO/CuO are predicted to have half-metallic properties, which are useful for spintronic applications.[29,30] Wurtzite-based superlattices are also interesting because two different interfaces are formed in them, which have different coordination environments and due to the different electronegativities of the metals surrounding the interfacial oxygen ions, polar bonds may be formed. In other words, the

---

[a] *Engineering Research Center of Micro-nano Optoelectronic Materials and Devices, Ministry of Education, Fujian Key Laboratory of Semiconductor Materials and Applications, CI Center for OSED, and Department of Physics, Xiamen University, Xiamen 361005, China. E-mail: hqwang@xmu.edu.cn, lty@xmu.edu.cn, jczheng@xmu.edu.cn*

[b] *Department of New Energy Science and Engineering, Xiamen University Malaysia, Sepang 43900, Malaysia*

[c] *Department of Applied Physics, The Hong Kong Polytechnic University, Hong Kong, China*

† Electronic supplementary information (ESI) available. See DOI: **https://doi.org/10.1039/d4cp00481g**

‡ These authors contributed equally.

formation of interfaces is related to the modification of the local symmetry of atomic arrangements and crystal potentials. It has been shown that the thermoelectric transport properties are mainly determined from the asymmetry of the electron states with respect to the Fermi energy.[31] It would be interesting to see how the asymmetries of the ZnO-based superlattice affect the electronic and magnetic properties. Moreover, interface states[1] may emerge in the superlattice and can be tuned by the thickness of the superlattice, thus creating a superlattice with unique electronic properties. Indeed, ZnO/w-MgO has been found to exhibit superior piezoelectric response.[32]

In this work, we combine wurtzite ZnO with a wurtzite form of FeO, *i.e.* w-FeO, to form $(\mathrm{ZnO})_n/(\text{w-FeO})_n$ (0001) superlattices (n = 1, 2, . . ., 6). First-principles calculations by Martín-García *et al.*[33] have confirmed that w-FeO is an antiferromagnetic conductor with an in-plane lattice constant that closely matches that of ZnO. Freestanding w-FeO has not been experimentally synthesized and is likely to be metastable and spontaneously transformed to the stable rocksalt FeO., It is likely that w-FeO can be grown and stabilized by using ZnO as the substrate. This has been shown possible in previous studies,[34–36] where heating ZnO with Fe deposition led to the formation of FeO. This superlattice combination is interesting due to the difference in their 3d orbitals: Zn is completely filled but Fe is only partially filled, which leads to net charge transfer through an interfacial O atom, and is likely to depend on the local interfacial environment. Moreover, w-FeO is predicted to be antiferromagnetic (AFM) while ZnO is a wide-bandgap semiconductor. Thus, there is a possibility of spin injection, as seen in the previously discussed combinations that have half-metallic properties[37] that are desirable for spintronic applications.

We constructed $(\mathrm{ZnO})_n/(\text{w-FeO})_n$ based on the in-plane lattice constant of ZnO and studied the energetics of the competing AFM and FM phases. The results revealed that the AFM phase is favoured for all values of n, with increasing energetic stability as n increases. We also analyzed the ionic charge population and magnetic moments for AFM and FM SLs with n = 6, which shows evidence of spin-polarized electron transfer across the interface from Fe to Zn, and the Zn ions acquire nonzero magnetic moments. However, due to the screening effect of the O ions, the internal ions farther away from the interface remain relatively unaffected. There are also clear differences between the two interfaces, with charge transfer being more pronounced at one interface than at the other.

2. Computational details

Spin-polarized density functional theory (DFT)[38] calculations were carried out on a plane-wave basis, as implemented in the Quantum ESPRESSO (QE)[39,40] code. In all calculations, we used the revised Perdew–Burke–Ernzerhof generalized gradient approximation[41] for solids (PBEsol)[42] and the projector augmented wave (PAW)[43,44] pseudopotential method with a high plane wave cutoff of 90 Ry to explicitly include the core wave function of the 3s and 3p orbitals of Fe. The Monkhorst–Pack k-point sampling scheme[45] is used for Brillouin zone integration and the k-point grid is selected such that its density is ~ 0.20 Å^{-1} in each direction. Additionally, DFT+U as implemented in QE is used to include the effect of strong correlation of Fe d-orbital electrons, and the Hubbard parameter U is set to 4.36 eV, as calculated using the HP code,[46,47] which employs density-functional perturbation theory to determine the Hubbard parameter. In order to make our results be more comparable with experimental results, we also performed additional calculations to correct the band gap of ZnO by applying on-site Hubbard U values of 10 eV to Zn-3d orbitals and 6.5 eV to O-2p orbitals,[48,49] respectively.

3. Results and discussion

3.1 Bulk ZnO and w-FeO

The relaxed lattice of bulk ZnO is shown in Fig. 1(a), with lattice parameters a = 3.23 Å and c = 5.24 Å, which are in good agreement with the experimental data[50,51] (a = 3.25 Å and c = 5.21 Å) and close to our previous GGA calculation results.[52–54] Fig. 1(d) displays its electronic band structure and density of states (DOS) exhibiting a direct band-gap E_g = 0.69 eV, which is much smaller compared to the previous DFT result of 1.51 eV,[55] but both are much lower than the experimental value of $\sim$3.4 eV[56,57] due to the typical band gap underestimation of standard DFT exchange–correlation (XC) functionals,[58] and PBEsol has also been proven to underestimate the band-gap calculated using only PBE.[59]

There are two possible magnetic phases for w-FeO: ferromagnetic (FM) and antiferromagnetic (AFM). The optimized lattice parameters and their relative energies are tabulated in Table 1, which also includes the results from the constrained a (= b) calculations discussed in the next paragraph. Clearly, the AFM phase is favoured over the FM phase, with a large difference of 160 meV per cell, and the planar lattice constant a of the former is also larger than that of the latter, but the converse is true for the vertical lattice constant c. Our value of a is 3.22 Å, close to 3.26 Å by Martín-García *et al.*,[33] but their reported c is 5.39 Å, which differs from our value of 5.50 Å by 2.6%. This could be due to a variety of reasons, such as the pseudopotential used, different Hubbard U values, and the chosen method.

The electronic band structures and density of states (DOS) of the different w-FeO phases are shown in Fig. 1(c) and (d). In both phases, w-FeO displays a metallic character. Near the Fermi level, the free electron parabolic-like dispersion is obvious for the majority spin (spin-up), while for the minority spin (spin-down), localized bands dominate. This suggests that the 4s orbital of Fe is responsible for the majority spin while the 3d orbital contributes to the localized bands for the minority spin. The presence of the Hubbard term penalizes the occupation of the minority spin, thereby shifting the energies of the minority 3d orbitals up while pulling them down in the case of the majority spin.

As the superlattice will be assembled with a fixed at that of ZnO, we also studied the w-FeO lattice with a = 3.23 Å fixed,

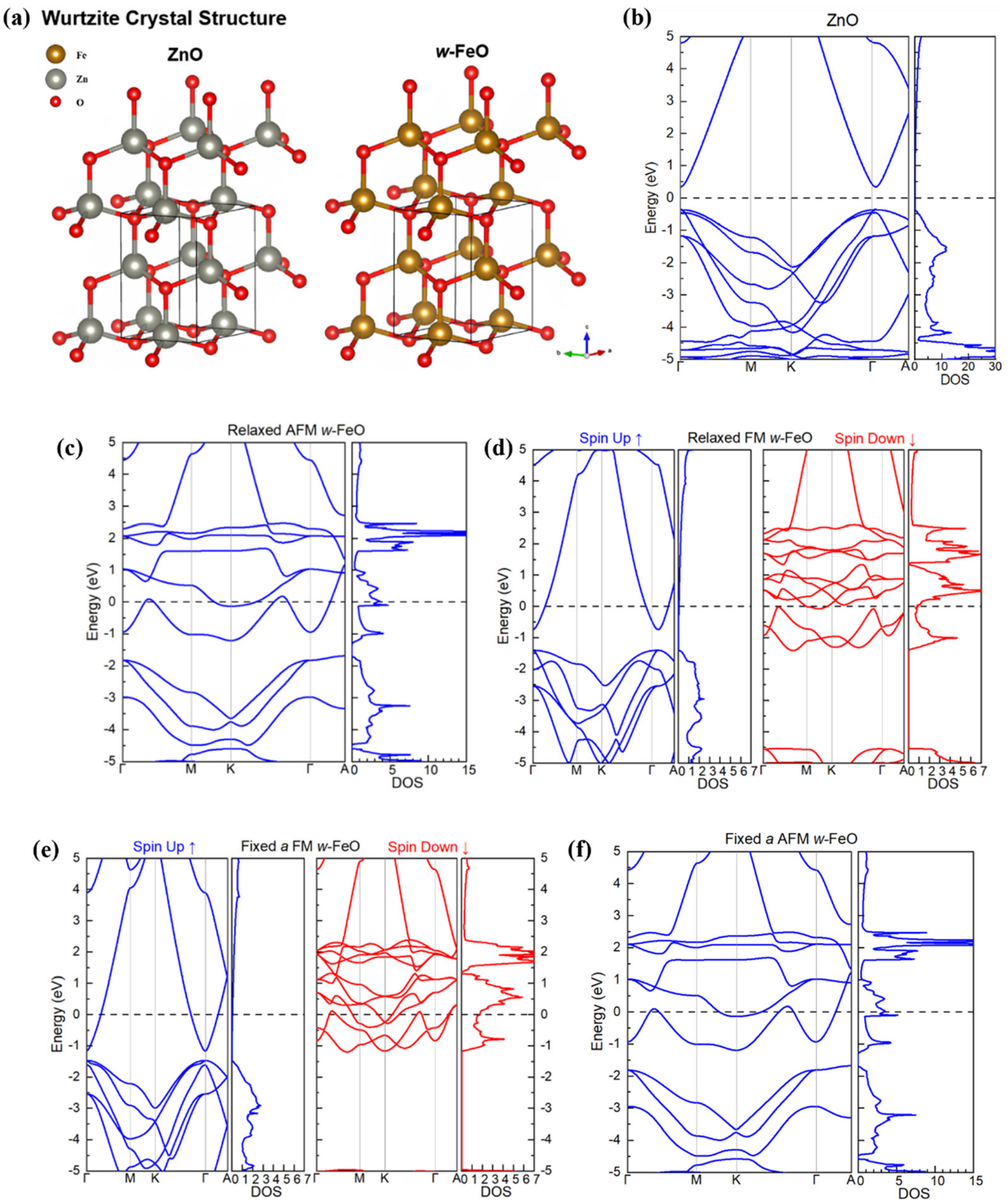

Fig. 1 Crystal structures of bulk ZnO (left) and bulk w-FeO (right) (a). Electronic band structure and density of states of ZnO (b) and w-FeO, fully relaxed lattice for AFM (c) and spin-polarized FM (d), and fixed *a* FM (e) and AFM (f).

Table 1 Lattice parameters and relative energies for different phases of w-FeO

w-FeO phase	*a* (Å)	*c* (Å)	Relative energy (meV per cell)
AFM	3.22 (relaxed) 3.23 (fixed)	5.53 5.50	0 1
FM	3.07 (relaxed) 3.23 (fixed)	5.81 5.50	160 240

equating to an in-plane biaxial tensile strain of about 0.3%, while the value of c and the atoms are allowed to relaxed completely, yielding $c = 5.50$ Å for both phases. The AFM phase is again favored over the FM phase, with a substantial difference of 239 meV per cell. As the strain induced for AFM w-FeO is minimal, the electronic properties of the structure remain almost the same, whereas, for FM, only the separation of the valence and conduction bands changed: decreased for majority spin and increased for minority spin. However, these changes occur below the Fermi level; hence, they have little impact on the overall electronic properties.

3.2 $(ZnO)_n/(w\text{-}FeO)_n$ superlattice: magnetic properties and charge transfer

We constructed a $(ZnO)_n/(w\text{-}FeO)_n$ superlattice with $n = 1, 2, 3, \ldots, 6$, assuming epitaxial growth on ZnO, with the in-plane lattice constant *a* fixed at 3.23 Å. Their crystal structures are shown in Fig. 2(a). For each *n*, we performed both antiferromagnetic and ferromagnetic calculations, where Fe has antiparallel and parallel spins with respect to the nearest Fe neighbour(s) along the superlattice, as shown in Fig. 2(b), respectively. Note that in the case of the odd *n* AFM phase, the AFM order is only locally realized as there is only a spin left uncancelled, which results in an overall FM magnetic moment.

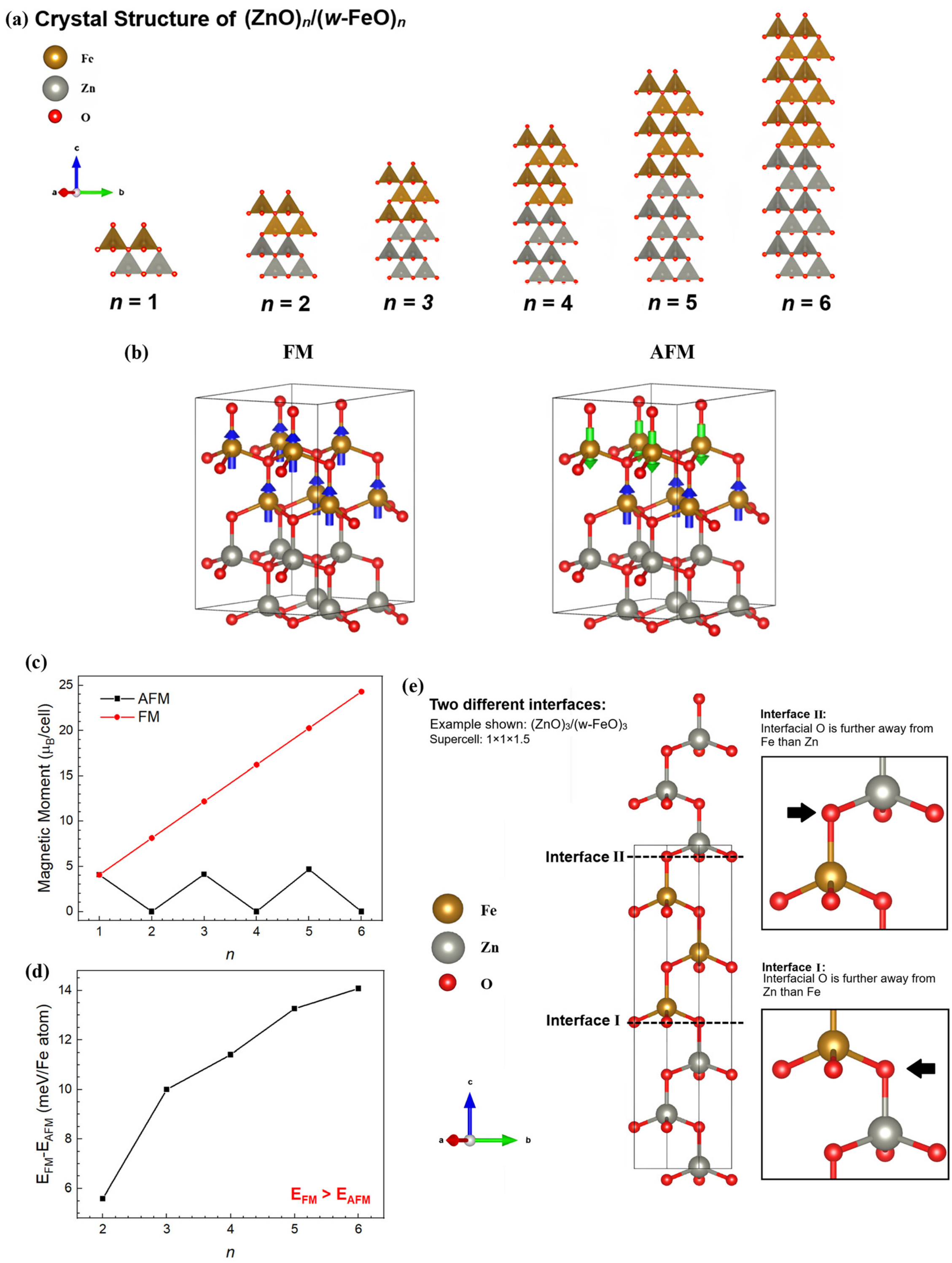

Fig. 2 (a) Crystal structure of the relaxed superlattice (SL) $(ZnO)_n/(w\text{-}FeO)_n$ for *n* = 1, 2, . . ., 6. The red spheres represent O atoms. The brown and silver tetrahedrons contain Fe and Zn atoms at their respective centers. The energies and magnetic moments of the AFM and FM states, depicted in (b), for each *n* are shown in (c) and (d), respectively. Two different interfaces (IFs) of the superlattices are highlighted in (e).

This is evident in Fig. 2(c), which shows that the magnetic moment of the AFM superlattice alternates between 0 and 4 μ_B per cell when n alternates between odd and even numbers. The energies for both FM and AFM phases with different thicknesses n are displayed in Fig. 2(d), where the AFM alignment gradually stabilizes energetically as n increases. This is likely caused by the increase of the bulk character of w-FeO, which strongly favours the AFM phase. As $n \to \infty$, we predict that the energy difference between the two magnetic phases will approach that of bulk w-FeO.

For $n > 1$, the SL has two different interfaces that have different local symmetries. As depicted in Fig. 2(d), the interfacial O ion is nearest to a Zn ion and three Fe ions for interface I (IF-I), while the opposite (O bonded with three Zn ions and one Fe ion) is true for interface II (IF-II). Fig. 3(b)–(e) show $n = 6$ AFM and FM magnetic moments and net charge population of atomic layers in the SL, which are labelled according to Fig. 3(a). Note that the values are obtained using atomic orbital projections, which are highly dependent on the basis sets used; thus, only the relative trends, but not absolute values, are meaningful. The trends of the Zn ions are similar in both phases, where the internal ions (Zn2 to Zn5) have almost constant charges and magnetic moments, whereas Zn1 and Zn6 have higher values. Inside the ZnO layers, the O ions (O1 to O5) have constant magnetic moments and charges, whereas in the FeO layers, O7 to O11 have decreased charges but increased magnetic moments. As the net charges of all O ions are positive, this implies that there is charge transfer from Zn and Fe ions to O ions, which is expected from the higher electronegativity of O (3.5) compared to Fe (1.83) and Zn (1.65). The higher difference in electronegativity causes a larger charge transferred from Zn, but the charge transferred from Fe is polarized, which results in a nonzero magnetic moment for the O ions that reside in the FeO layers.

At the interfaces, the O ions are bound to different numbers of Zn and Fe ions; thus, they possess different magnetic moments and charges. The charges and magnetic moments of O12 at IF II are similar for both AFM and FM phases, but at IF I, O6 has a higher magnetic moment in the AFM phase, despite having the same charge. The trend in the Fe ions is much more varied; the internal Fe charges and magnetic moments are nearly constant in the AFM phase but vary in the FM phase. In the AFM phase, the interfacial Fe1 and Fe6 have lower charges but higher magnetic moments, compared to the inner Fe ions; however, in the FM phase, this is only true for Fe6: Fe1 at IF I has a higher charge and a lower magnetic moment. This indicates that the charge transferred away is of minority spin, thereby increasing the magnetic moment in Fe ions and O ions, which gained polarized charge. The different local environments at IF I and IF II caused notable differences in charges and magnetic moments. The O ion is bound to more Fe ions at IF I than at IF II, which increases the polarized charge received from Fe ions, and subsequently results in a higher magnetic moment but lower charge received, as it is bonded to fewer Zn ions, which is more electropositive.

3.3 $(ZnO)_n/(w\text{-}FeO)_n$ superlattice: spin-dependent electronic properties

The electronic band structures and DOS of the SL with all n and both AFM and FM phases are shown in Fig. 4(b)–(g), where the Brillouin zone path depicted in Fig. 4(a) is adopted. For all n and magnetic phases, the superlattices are metallic and the AFM band structure closely resembles that of bulk AFM w-FeO. Overall, the energy bands retain the free-electron-like behaviour close to the Fermi level, but they break due to the interaction with the Fe 3d orbitals, except in the majority spin (spin-up) of the FM phase. Similar to the FM w-FeO, the

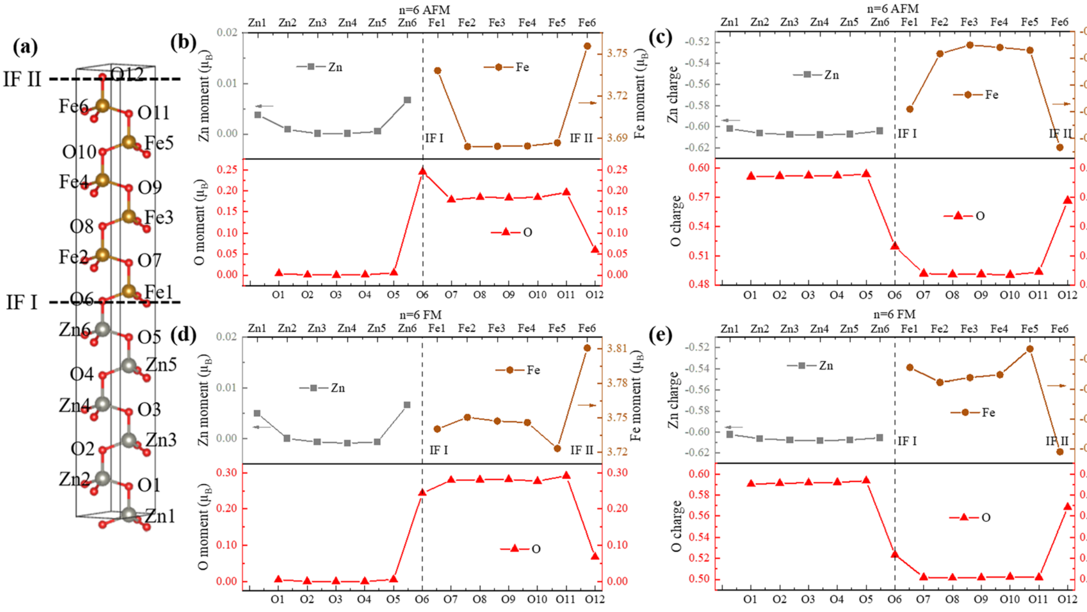

Fig. 3 (a) Atomic configuration of $(ZnO)_6/(w\text{-}FeO)_6$ with each atom and interface (IF) labelled. The Löwdin net charge population and magnetic moments for the AFM and FM phases are shown in (b) and (c) and (d) and (e), respectively.

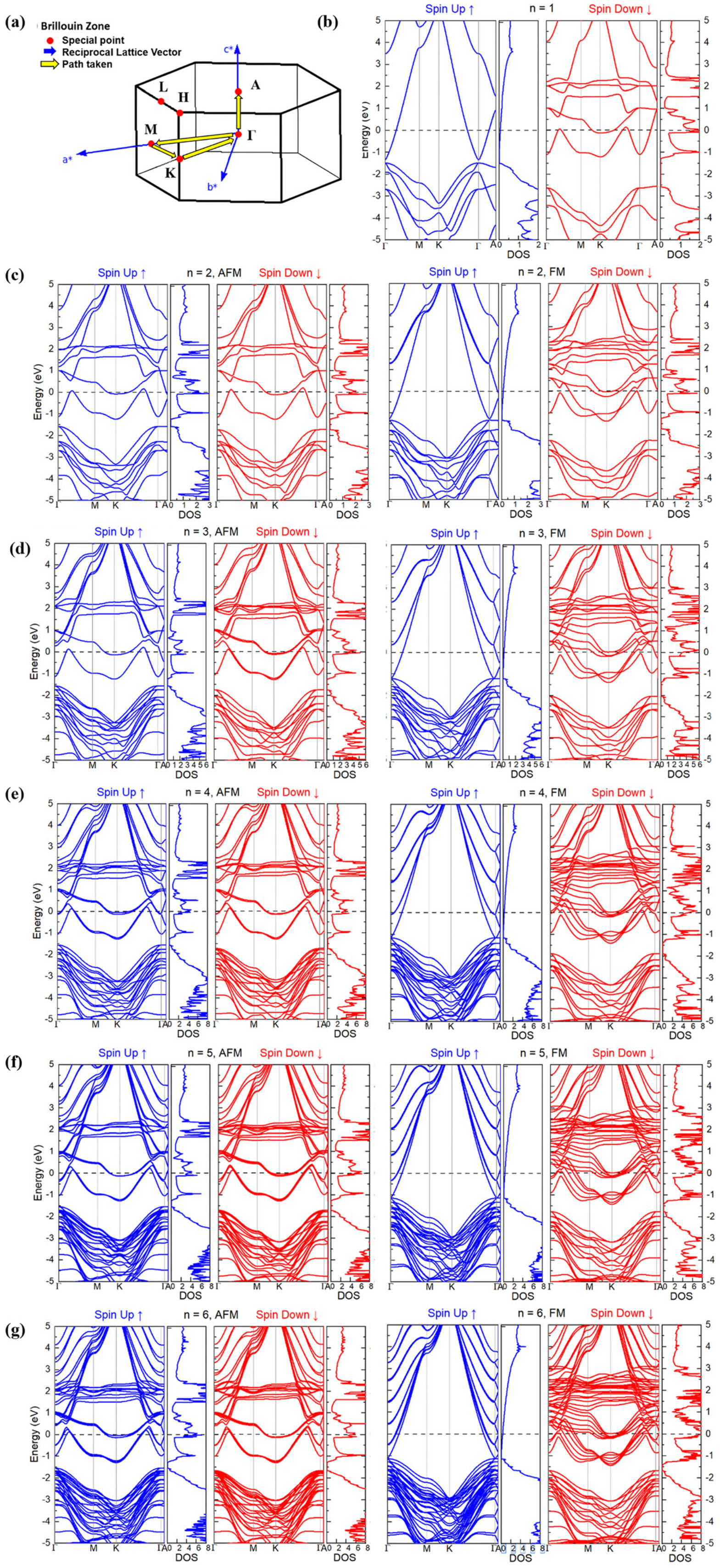

Fig. 4 (a) The Brillouin zone path taken for electronic band structure plot of $(ZnO)_n/(w\text{-}FeO)_n$ for all *n* and both AFM and FM phases, as shown from (b) to (g) along with the density of states, spin-polarized.

characteristics of the energy levels between the majority and minority spins are in stark contrast: they are delocalized for the majority spin and strongly localized for the minority spin, which will result in interesting spin-dependent transport properties.

The splitting of bands close to the Fermi level can be observed in the minority spin FM band structure, which remains highly degenerate in the case of AFM. The difference between odd n and even n can be observed in the AFM band structure: at an energy of 2 eV, the bands for the minority spin (spin-down) are thicker than those for the majority spin (spin-up). This is caused by the addition of Fe atoms with a majority spin, creating an imbalance between the majority and minority spin orbitals. For even n, we can notice differences between the two spins in the DOS, especially around 2 eV, which can be attributed to the difference in the two interfaces.

In Fig. 5, we display the projected valence orbital band structures for the $n = 6$ superlattice in the FM phase, demonstrating the notable differences between the atoms around interfaces I and II, which are less distinct in the AFM phase. Here, the reciprocal space path is truncated as the segment of Γ to A does not contain new information. At the Fermi level, we can see a clear shift of the energy level at the K point of spin-down projected Fe orbitals, where at interface I, the energy band is below the Fermi level while at interface II it is above and thus unoccupied. This corroborates the Fe charge shown in Fig. 3(e), in which the charge of Fe at interface I is higher than that at interface II by about 0.06 e. Furthermore, as this missing charge originates from the minority spin, the magnetic moment increases, matching the magnetic moment data in Fig. 3(d). The most distinct difference for Zn ions is far above the Fermi level, and is almost imperceptible near the Fermi level, but the small differences also match their charge differences. For O ions, a stark difference can be seen: the states below the Fermi level are much more abundant for IF II, which is again reflected in the charge differences. More detailed atomic-layer projected spin-polarized density of states for AFM and FM $(\mathrm{ZnO})_n/(\mathrm{w\text{-}FeO})_n$ when $n = 1, 2, \ldots, 6$ are presented in Fig. S1 (ESI†), which clearly shows the differences in the spin-dependent electronic properties and differences between IF I and II.

3.4 Effects of adding Hubbard U to Zn-3d and O-2p orbitals

In the previous section, the obtained ZnO band gap was far lower than the experimental value. This is in line with the data collected in a previous review,[49] where using DFT alone far underestimates its band gap, which can be corrected by enabling the Hubbard correction for both Zn and O species.[49,60] Here, we re-calculated the band gap using $U = 10$ eV and 6.5 eV for Zn-3d and O-2p orbitals, respectively, as was used in Harun *et al.*,[48] which utilized the same type of functional (PBEsol). The band gap we obtained is 3.05 eV, which is in good agreement with their band gap of 3.102 eV and much closer to the experimental value of ∼3.4 eV.

Using this setting, we repeated the band structure computation for all SL, and plotted both AFM and FM phases for $n = 6$ in Fig. 6, with the rest of the n in Fig. S2 (ESI†). For both phases and all n, there are no significant changes at the Fermi level, and no band gap is opened. In both AFM and FM phases, the major difference is the opening or widening of the band gap ∼2 eV below the Fermi level, which does not alter the electronic conduction properties near the Fermi level. Additionally, there is further splitting of bands located below −2 eV, which is more noticeable in the AFM phase.

The lack of change around the Fermi level is expected as the bands in this region are made up of Fe-3d and Zn-4s orbitals, as

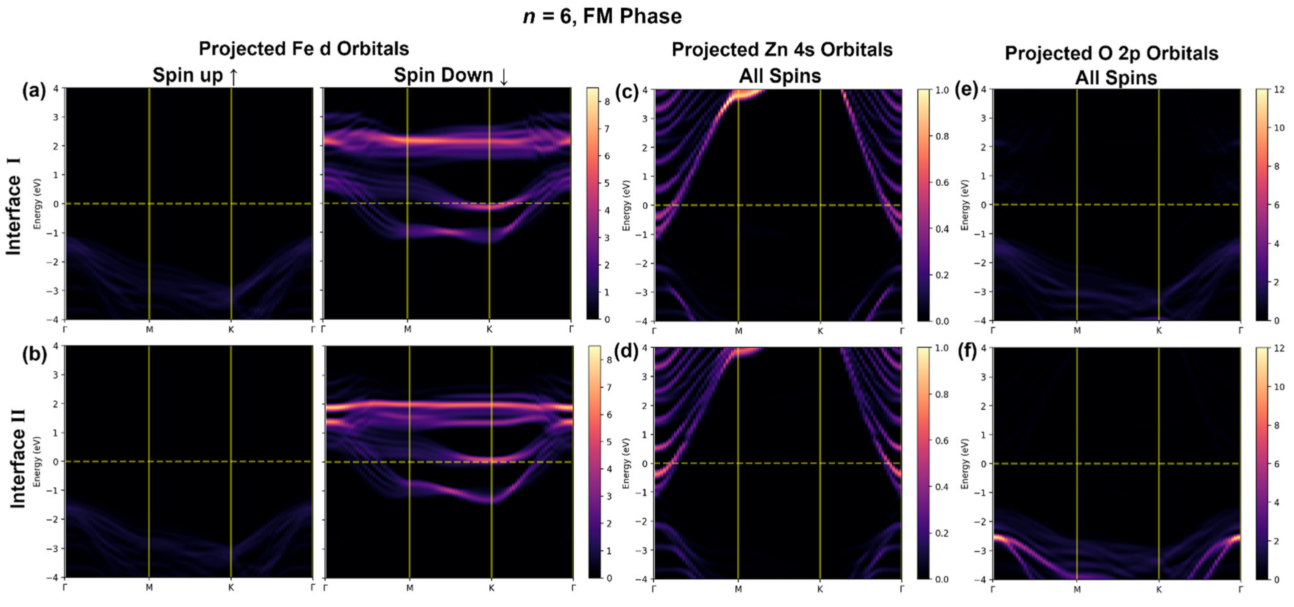

Fig. 5 Projected orbitals in the band structures for $n = 6$ FM phase at interfaces I and II: spin-polarized projected Fe 3d orbitals (a) and (b), projected Zn 4s orbitals (c) and (d), and projected O 2p orbitals (e) and (f).

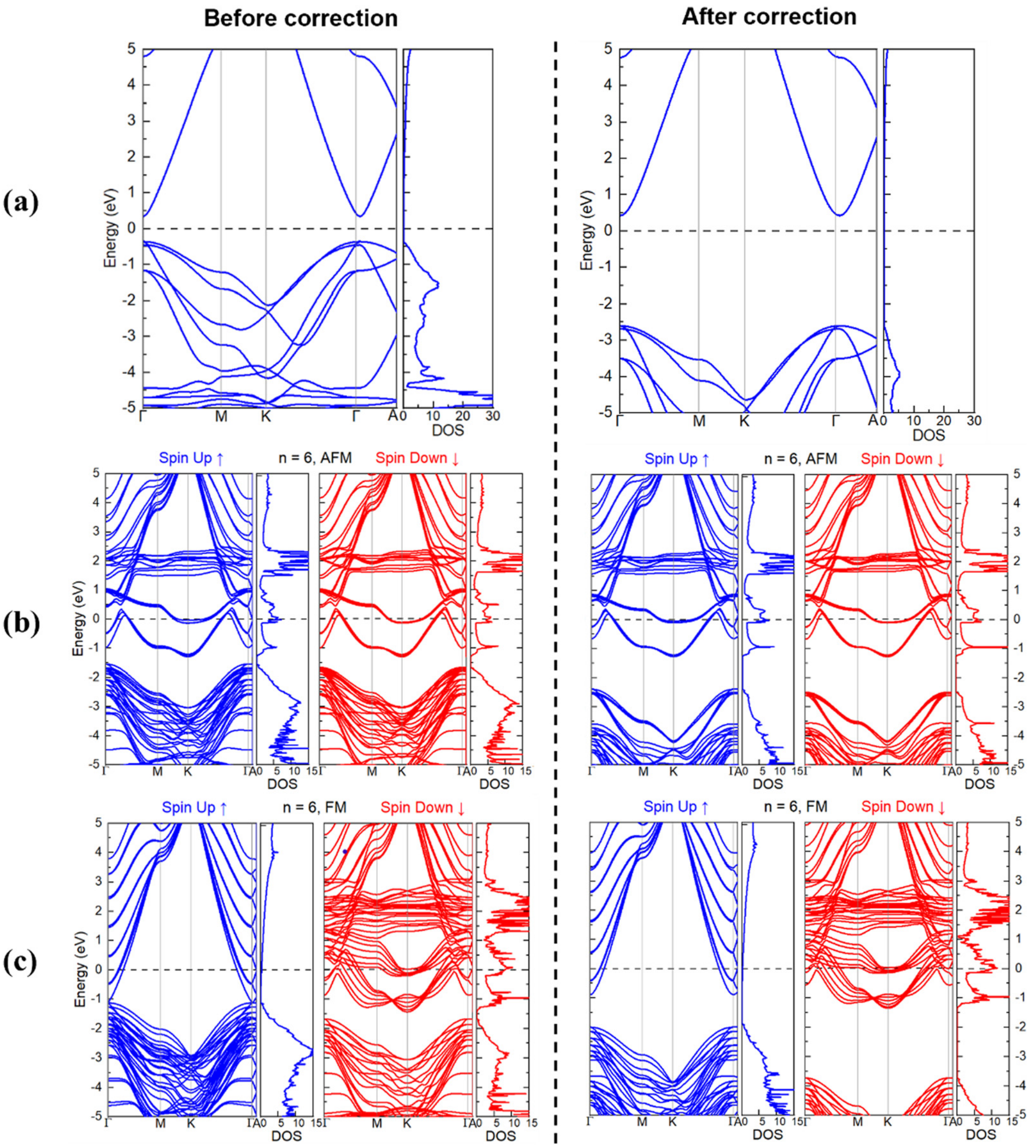

Fig. 6 Electronic band structure and density of states with and without Hubbard *U* correction added to Zn-3d and O-2p orbitals, for ZnO (a), and AFM (b) and FM (c) phases of $(ZnO)_6/(w\text{-}FeO)_6$.

can be seen in Fig. 6, which are left unchanged. After adding the Hubbard correction, the bands 2 eV below the Fermi level are shifted downward because these bands originate mainly from the O-2p and Zn-3d orbitals. The split among the bands is then due to the different amounts of Hubbard *U* added to the respective orbitals, and the individual orbitals are shifted by different magnitudes.

With the inclusion of extra Hubbard correction, we expect the charge transfers and hence the magnetic moment to be affected, and we have shown the comparison of the charge and magnetic moments in Fig. S3 (ESI†) for $n = 6$ SL. Overall, the charge transferred to all O ions increased by roughly 0.10 e, while the opposite was true for Fe and Zn ions. Despite the increased charge transfer, the O ions in the FeO layers have a reduced magnetic moment, while the Fe ions have the opposite trend. At both interfaces, the magnetic moments of the Zn ions decreased, which could be due to the increased screening of O ions. The atomic-layer projected density of states, for $n = 6$ SL, namely, $(ZnO)_6/(w\text{-}FeO)_6$, as shown in Fig. S4 (ESI†), clearly shows the difference in electronic structures between the majority and minority spins, as well as those between IF I and II.

3.5 Effects of different spin states and ordering

For completeness, we will also discuss the different FM spin states and AFM spin ordering of the SL in a larger supercell (2 × 2 × 1). There are three possible spin states for Fe^{2+} (d^6): low, intermediate, and high, which correspond to the nonmagnetic ($S = 0$), partially ($S = 1$), and fully ($S = 2$) magnetized phases. As illustrated in Fig. 7, there are four AFM spin orderings, denoted as A-, C-, and G-types. In previous sections, the FM spin state and AFM spin ordering considered are high and of A-type

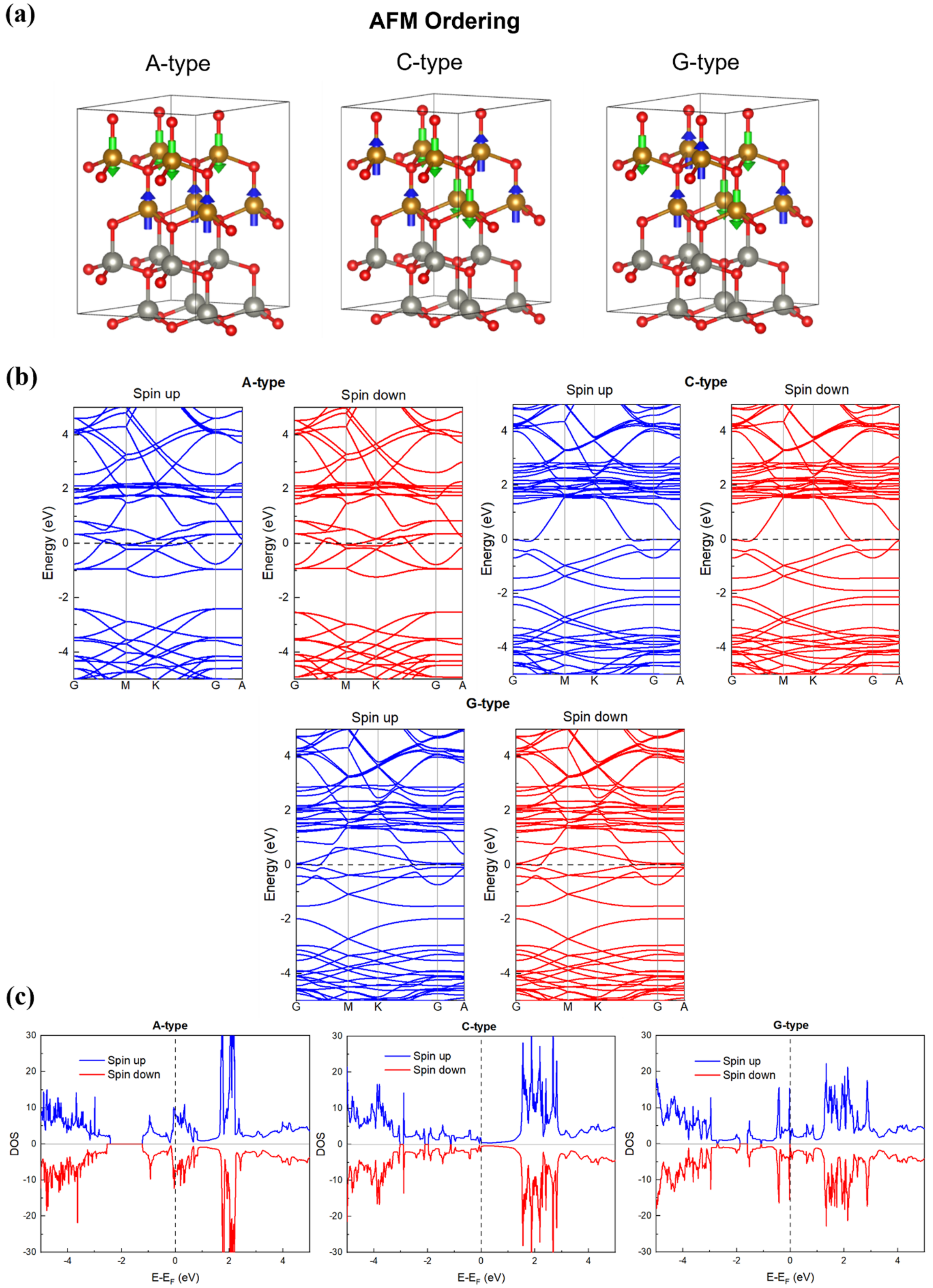

Fig. 7 (a) A-, C-, and G-type spin orderings shown in a 2 × 2 × 1 supercell for $(ZnO)_2/(w\text{-}FeO)_2$. Their respective band structures and density of states are shown separately in (b) and (c), respectively.

ordering, respectively. The energy comparison is shown in Table 2, and it is clear that the high-spin state is the most stable for FM, while the C-type ordering is the most favorable AFM ordering, followed by the G-type and then the A-type. C-type ordering has the highest amount of nearest-neighbour opposite-spin pairing, while A-type has the least, with G-type

Table 2 Relative energy for different FM spin states and AFM spin orderings for n = 2 SL

FM spin state	Relative energy (eV/Fe atom)	AFM spin ordering	Relative energy (eV/Fe atom)
Low	1.20	A	0.58
Intermediate	0.65	C	0.00
High	0.00	G	0.49

in the middle. If we examine the spin-order-induced local symmetry, for example, taking oxygen as the center of the FeO_4 tetrahedron, there are three Fe↓ and one Fe↑ for the A-type (Fig. 7(a)), two Fe↓ and two Fe↑ for the C-type, and one Fe↓ and three Fe↑ for the G-type. This means that the C-type has the smallest amount of local ferromagnetism, unlike the A-type, which is ferromagnetic in each layer. The maximization of antiferromagnetism is likely the reason it is the most stable.

The band structure and density of states for different AFM spin orderings are shown in Fig. 7(b) and (c), respectively. Note that the A-type band structure shown here is different from that in Fig. 4 due to the band folding caused by the larger supercell used. The most noticeable difference in the C-type band structures is the downshifting of the bands near the Fermi level, which removes the wide gap of about 1.5 eV below the Fermi level. This can also be seen in the G-type band structure, but to a lesser extent. The DOS of the C-type also reflects this: at a Fermi level and up to about 1.8 eV, the DOS is minimal compared to the A- and G-types. This difference causes a reduction in the anti-bonding electronic energy, resulting in a lower energy for the C-type. The SL remains metallic for all types. The downshifting of the localized bands at the Fermi level can be understood as the reduction of Pauli repulsion, as the 3d electrons possessing similar quantum states and spin among the nearest neighbors have been minimized.

To understand the effect of C-type AFM ordering on the charge transfer and magnetic moment, we also investigated the n = 4 SL, as it has a sufficient thickness such that there is a contrast between interfaces I and II. In Fig. S5 (ESI†), we show the atomic arrangement and spin alignment, and the net charge and magnetic moment of each atomic layer. For type C AFM ordering, a clear distinction between interfaces I and II can be observed, which is in good agreement with the other magnetic orderings but with different details. Within each layer, the atomic charge and magnetic moment are constant. The trend for net charge is similar to that of A-type, except for the Fe ions, where at IF II, the net charge is the same as that of the bulk Fe ions. Despite having a similar magnitude of net charge, the O ions have substantially a lower magnetic moment. A plausible explanation is that the alternating spins within a layer contribute charges of opposite spins to the O ions, thereby reducing the magnetization of the O ions and becoming negligible.

4. Conclusions

In summary, we have performed spin-polarized density functional theory calculations to investigate the detailed structural, electronic and magnetic properties of novel superlattices constructed using a wide-band-gap semiconductor, ZnO, and typical multiferroics, FeO. Our calculations showed that the AFM phases of $(ZnO)_n/(w\text{-}FeO)_n$ are energetically more favorable than the FM phase. In terms of spin states and ordering in SL, it is found that the high-spin state is the most stable state for FM, while the C-type ordering is the most favorable AFM ordering. The magnetic moments and ionic charge population of SLs are analyzed. Spin-polarized electron transfer across the interface from Fe to Zn is observed, and nonzero magnetic moments are found for Zn and O at the interfaces. Two different interfaces in the $(ZnO)_n/(w\text{-}FeO)_n$ superlattices have been identified, which show very different magnetic and electronic properties. These effects arise from variations in the Fe/Zn distribution across different interfaces or from the spin ordering of Fe within the superlattice structure. The oxygen ions have much higher interface-induced magnetic moments at interface I (oxygen bonded with three Fe ions and one Zn ion) than at interface II (oxygen bonded with one Fe ion and three Zn ions). For all n and magnetic phases, the superlattices showed metallic band structures. It was also found that, in the case of the ferromagnetic phase, the electrons are more delocalized for the majority spin but strongly localized for the minority spin, which results in interesting spin-dependent transport properties. The interesting electronic and magnetic features of the $(ZnO)_n/(w\text{-}FeO)_n$ superlattices may shed some light on the design of novel devices with a combination of semiconductors and functional materials such as multiferroics. Furthermore, given the rapid development of machine learning in materials science,[61] one can expect that research on superlattices including $(ZnO)n/(w\text{-}FeO)n$ and other semiconductor/multiferroic superlattices or interfaces can benefit from advances in artificial intelligence.

Abbreviations

SL	Superlattice
FM	Ferromagnetic
AFM	Antiferromagnetic

Conflicts of interest

The authors declare no conflict of interest.

Acknowledgements

This research is supported by the Ministry of Higher Education Malaysia through the Fundamental Research Grant Scheme (FRGS/1/2021/STG07/XMU/01/1).

References

1 H.-Q. Wang, J. Xu, X. Lin, Y. Li, J. Kang and J.-C. Zheng, Determination of the embedded electronic states at nanoscale interface via surface-sensitive photoemission spectroscopy, *Light: Sci. Appl.*, 2021, **10**, 153.

2 J. Mannhart, D. H. A. Blank, H. Y. Hwang, A. J. Millis and J. M. Triscone, Two-Dimensional Electron Gases at Oxide Interfaces, *MRS Bull.*, 2008, **33**, 1027–1034.

3 J. Chakhalian, A. J. Millis and J. Rondinelli, Whither the oxide interface, *Nat. Mater.*, 2012, **11**, 92–94.

4 F. Ernst, Metal-oxide interfaces, *Mater. Sci. Eng., R*, 1995, **14**, 97–156.

5 J. Mannhart and D. G. Schlom, Oxide Interfaces—An Opportunity for Electronics, *Science*, 2010, **327**, 1607–1611.

6 H. Zhou, L. Wu, H.-Q. Wang, J.-C. Zheng, L. Zhang, K. Kisslinger, Y. Li, Z. Wang, H. Cheng, S. Ke, Y. Li, J. Kang and Y. Zhu, Interfaces between hexagonal and cubic oxides and their structure alternatives, *Nat. Commun.*, 2017, **8**, 1474.

7 H. Y. Hwang, Y. Iwasa, M. Kawasaki, B. Keimer, N. Nagaosa and Y. Tokura, Emergent phenomena at oxide interfaces, *Nat. Mater.*, 2012, **11**, 103–113.

8 L. Bjaalie, B. Himmetoglu, L. Weston, A. Janotti and C. G. V. de Walle, Oxide interfaces for novel electronic applications, *New J. Phys.*, 2014, **16**, 025005.

9 F. Hellman, A. Hoffmann, Y. Tserkovnyak, G. S. D. Beach, E. E. Fullerton, C. Leighton, A. H. MacDonald, D. C. Ralph, D. A. Arena, H. A. Dürr, P. Fischer, J. Grollier, J. P. Heremans, T. Jungwirth, A. V. Kimel, B. Koopmans, I. N. Krivorotov, S. J. May, A. K. Petford-Long, J. M. Rondinelli, N. Samarth, I. K. Schuller, A. N. Slavin, M. D. Stiles, O. Tchernyshyov, A. Thiaville and B. L. Zink, Interface-induced phenomena in magnetism, *Rev. Mod. Phys.*, 2017, **89**, 025006.

10 D. L. Smith and C. Mailhiot, Theory of semiconductor superlattice electronic structure, *Rev. Mod. Phys.*, 1990, **62**, 173–234.

11 N. Ya. Fogel, E. I. Buchstab, Y. V. Bomze, O. I. Yuzephovich, A. Y. Sipatov, E. A. Pashitskii, A. Danilov, V. Langer, R. I. Shekhter and M. Jonson, Interfacial superconductivity in semiconducting monochalcogenide superlattices, *Phys. Rev. B: Condens. Matter Mater. Phys.*, 2002, **66**, 174513.

12 G. Zhou, F. Jiang, J. Zang, Z. Quan and X. Xu, Observation of Superconductivity in the $LaNiO_3/La_{0.7}Sr_{0.3}MnO_3$ Superlattice, *ACS Appl. Mater. Interfaces*, 2018, **10**, 1463–1467.

13 K. S. Takahashi, M. Kawasaki and Y. Tokura, Interface ferromagnetism in oxide superlattices of $CaMnO_3/CaRuO_3$, *Appl. Phys. Lett.*, 2001, **79**, 1324–1326.

14 R. E. Camley, Properties of magnetic superlattices with antiferromagnetic interfacial coupling: Magnetization, susceptibility, and compensation points, *Phys. Rev. B: Condens. Matter Mater. Phys.*, 1989, **39**, 12316–12319.

15 J. Lee, N. Sai, T. Cai, Q. Niu and A. A. Demkov, Interfacial magnetoelectric coupling in tricomponent superlattices, *Phys. Rev. B: Condens. Matter Mater. Phys.*, 2010, **81**, 144425.

16 B. D. Qu, W. L. Zhong and R. H. Prince, Interfacial coupling in ferroelectric superlattices, *Phys. Rev. B: Condens. Matter Mater. Phys.*, 1997, **55**, 11218–11224.

17 L. Zhang, T.-Y. Lü, H.-Q. Wang, W.-X. Zhang, S.-W. Yang and J.-C. Zheng, First principles studies on the thermoelectric properties of $(SrO)_m(SrTiO_3)_n$ superlattice, *RSC Adv.*, 2016, **6**, 102172.

18 B. Zhang, L. Wu, J. Zheng, P. Yang, X. Yu, J. Ding, S. M. Heald, R. A. Rosenberg, T. V. Venkatesan, J. Chen, C.-J. Sun, Y. Zhu and G. M. Chow, Control of magnetic anisotropy by orbital hybridization with charge transfer in $(La_{0.67}Sr_{0.33}MnO_3)_n/(SrTiO_3)_n$ superlattice, *NPG Asia Mater.*, 2018, **10**, 931–942.

19 W. Zhang, F.-Y. Du, Y. Dai and J.-C. Zheng, Strain engineering of Li^+ ion migration in olivine phosphate cathode materials $LiMPO_4$ (M = Mn, Fe, Co) and $(LiFePO_4)_n(LiMnPO_4)_m$ superlattices, *Phys. Chem. Chem. Phys.*, 2023, **25**, 6142–6152.

20 M. Courel, J. C. Rimada and L. Hernández, AlGaAs/GaAs superlattice solar cells, *Prog. Photovoltaics Res. Appl.*, 2013, **21**, 276–282.

21 Y. Lei, Y. Li, C. Lu, Q. Yan, Y. Wu, F. Babbe, H. Gong, S. Zhang, J. Zhou, R. Wang, R. Zhang, Y. Chen, H. Tsai, Y. Gu, H. Hu, Y.-H. Lo, W. Nie, T. Lee, J. Luo, K. Yang, K.-I. Jang and S. Xu, Perovskite superlattices with efficient carrier dynamics, *Nature*, 2022, **608**, 317–323.

22 M. S. Gudiksen, L. J. Lauhon, J. Wang, D. C. Smith and C. M. Lieber, Growth of nanowire superlattice structures for nanoscale photonics and electronics, *Nature*, 2002, **415**, 617–620.

23 H. Chen, P. Yan, J. Li, C. He, T. Ouyang, C. Zhang, C. Tang and J. Zhong, Tunable photoelectronic properties of hydrogenated-silicene/halogenated-silicene superlattices for water splitting, *J. Appl. Phys.*, 2020, **127**, 084301.

24 Y.-S. Kim, C.-H. Ri, U.-H. Ko, Y.-H. Kye, U.-G. Jong and C.-J. Yu, Interfacial Enhancement of Photovoltaic Performance in $MAPbI_3/CsPbI_3$ Superlattice, *ACS Appl. Mater. Interfaces*, 2021, **13**, 14679–14687.

25 A. H. Ramelan, S. Wahyuningsih, H. Munawaroh and R. Narayan, ZnO wide band-gap semiconductors preparation for optoelectronic devices, *IOP Conf. Ser.: Mater. Sci. Eng.*, 2017, **176**, 012008.

26 A. Di Mauro, M. E. Fragalà, V. Privitera and G. Impellizzeri, ZnO for application in photocatalysis: From thin films to nanostructures, *Mater. Sci. Semicond. Process.*, 2017, **69**, 44–51.

27 M. Benlamri, B. D. Wiltshire, Y. Zhang, N. Mahdi, K. Shankar and D. W. Barlage, High Breakdown Strength Schottky Diodes Made from Electrodeposited ZnO for Power Electronics Applications, *ACS Appl. Electron. Mater.*, 2019, **1**, 13–17.

28 C. Klingshirn, ZnO: Material, Physics and Applications, *ChemPhysChem*, 2007, **8**, 782–803.

29 Z. Chen, L. Miao and X. Miao, Half-metallicity of wurtzite NiO and w-NiO/ZnO (0001) interface: First principles simulation, *AIP Adv.*, 2011, **1**, 022124.

30 A. Zaoui, M. Ferhat and R. Ahuja, Magnetic properties of $(ZnO)_1/(CuO)_1$ (001) superlattice, *Appl. Phys. Lett.*, 2009, **94**, 102102.

31 J.-C. Zheng, Asymmetrical Transport Distribution Function: Skewness as a Key to Enhance Thermoelectric Performance, *Research*, 2022, **2022**, 9867639.

32 X. Yang, M. Hu, T. Su, X. Ma, Y. Chen, X. Kong and W. Ren, Volume-matched ferroelectric and piezoelectric ZnO/MgO superlattice, *J. Alloys Compd.*, 2021, **876**, 160167.

33 L. Martín-García, I. Bernal-Villamil, M. Oujja, E. Carrasco, R. Gargallo-Caballero, M. Castillejo, J. F. Marco, S. Gallego and J. de la Figuera, Unconventional properties of nanometric FeO(111) films on Ru(0001): stoichiometry and surface structure, *J. Mater. Chem. C*, 2016, **4**, 1850–1859.

34 W.-C. Lin, P.-C. Chang, C.-J. Tsai, T.-C. Hsieh and F.-Y. Lo, Magnetism modulation of Fe/ZnO heterostructure by interface oxidation, *Appl. Phys. Lett.*, 2013, **103**, 212405.

35 D. Wett, A. Demund, H. Schmidt and R. Szargan, The Fe/ZnO(0001) interface: Formation and thermal stability, *Appl. Surf. Sci.*, 2008, **254**, 2309–2318.

36 A. Demund, D. Wett and R. Szargan, Study of formation and thermal stability of the Fe/ZnO(000-1) interface, *Surf. Interface Anal.*, 2008, **40**, 27–36.

37 J.-C. Zheng and J. W. Davenport, Ferromagnetism and stability of half-metallic MnSb and MnBi in the strained zinc blende structure: Predictions from full potential and pseudopotential calculations, *Phys. Rev. B: Condens. Matter Mater. Phys.*, 2004, **69**, 144415.

38 P. Hohenberg and W. Kohn, Inhomogeneous Electron Gas, *Phys. Rev.*, 1964, **136**, B864–B871.

39 P. Giannozzi, S. Baroni, N. Bonini, M. Calandra, R. Car, C. Cavazzoni, D. Ceresoli, G. L. Chiarotti, M. Cococcioni, I. Dabo, A. D. Corso, S. de Gironcoli, S. Fabris, G. Fratesi, R. Gebauer, U. Gerstmann, C. Gougoussis, A. Kokalj, M. Lazzeri, L. Martin-Samos, N. Marzari, F. Mauri, R. Mazzarello, S. Paolini, A. Pasquarello, L. Paulatto, C. Sbraccia, S. Scandolo, G. Sclauzero, A. P. Seitsonen, A. Smogunov, P. Umari and R. M. Wentzcovitch, QUANTUM ESPRESSO: a modular and open-source software project for quantum simulations of materials, *J. Phys.: Condens. Matter*, 2009, **21**, 395502.

40 P. Giannozzi, O. Andreussi, T. Brumme, O. Bunau, M. B. Nardelli, M. Calandra, R. Car, C. Cavazzoni, D. Ceresoli, M. Cococcioni, N. Colonna, I. Carnimeo, A. D. Corso, S. de Gironcoli, P. Delugas, R. A. DiStasio, A. Ferretti, A. Floris, G. Fratesi, G. Fugallo, R. Gebauer, U. Gerstmann, F. Giustino, T. Gorni, J. Jia, M. Kawamura, H.-Y. Ko, A. Kokalj, E. Küçükbenli, M. Lazzeri, M. Marsili, N. Marzari, F. Mauri, N. L. Nguyen, H.-V. Nguyen, A. Otero-de-la-Roza, L. Paulatto, S. Poncé, D. Rocca, R. Sabatini, B. Santra, M. Schlipf, A. P. Seitsonen, A. Smogunov, I. Timrov, T. Thonhauser, P. Umari, N. Vast, X. Wu and S. Baroni, Advanced capabilities for materials modelling with Quantum ESPRESSO, *J. Phys.: Condens. Matter*, 2017, **29**, 465901.

41 J. P. Perdew, K. Burke and M. Ernzerhof, Generalized Gradient Approximation Made Simple, *Phys. Rev. Lett.*, 1996, **77**, 3865–3868.

42 J. P. Perdew, A. Ruzsinszky, G. I. Csonka, O. A. Vydrov, G. E. Scuseria, L. A. Constantin, X. Zhou and K. Burke, Restoring the Density-Gradient Expansion for Exchange in Solids and Surfaces, *Phys. Rev. Lett.*, 2008, **100**, 136406.

43 P. E. Blöchl, Projector augmented-wave method, *Phys. Rev. B: Condens. Matter Mater. Phys.*, 1994, **50**, 17953–17979.

44 G. Kresse and D. Joubert, From ultrasoft pseudopotentials to the projector augmented-wave method, *Phys. Rev. B: Condens. Matter Mater. Phys.*, 1999, **59**, 1758–1775.

45 H. J. Monkhorst and J. D. Pack, Special points for Brillouin-zone integrations, *Phys. Rev. B: Solid State*, 1976, **13**, 5188–5192.

46 I. Timrov, N. Marzari and M. Cococcioni, Hubbard parameters from density-functional perturbation theory, *Phys. Rev. B: Condens. Matter Mater. Phys.*, 2018, **98**, 085127.

47 I. Timrov, N. Marzari and M. Cococcioni, Self-consistent Hubbard parameters from density-functional perturbation theory in the ultrasoft and projector-augmented wave formulations, *Phys. Rev. B*, 2021, **103**, 045141.

48 K. Harun, M. K. Yaakob, M. F. M. Taib, B. Sahraoui, Z. A. Ahmad and A. A. Mohamad, Efficient diagnostics of the electronic and optical properties of defective ZnO nanoparticles synthesized using the sol–gel method: experimental and theoretical studies, *Mater. Res. Express*, 2017, **4**, 085908.

49 K. Harun, N. A. Salleh, B. Deghfel, M. K. Yaakob and A. A. Mohamad, DFT+U calculations for electronic, structural, and optical properties of ZnO wurtzite structure: A review, *Results Phys.*, 2020, **16**, 102829.

50 R. B. Heller, J. McGannon and A. H. Weber, Precision Determination of the Lattice Constants of Zinc Oxide, *J. Appl. Phys.*, 2004, **21**, 1283–1284.

51 E. H. Kisi and M. M. Elcombe, U parameters for the wurtzite structure of ZnS and ZnO using powder neutron diffraction, *Acta Crystallogr., Sect. C: Cryst. Struct. Commun.*, 1989, **45**, 1867–1870.

52 X. Shen, P. B. Allen, J. T. Muckerman, J. W. Davenport and J.-C. Zheng, Wire versus Tube: Stability of Small One-Dimensional ZnO Nanostructures, *Nano Lett.*, 2007, **7**, 2267–2271.

53 Y. Zhang, Y.-H. Wen, J.-C. Zheng and Z.-Z. Zhu, Direct to indirect band gap transition in ultrathin ZnO nanowires under uniaxial compression, *Appl. Phys. Lett.*, 2009, **94**, 113114.

54 Z. Huang, T.-Y. Lü, H.-Q. Wang and J.-C. Zheng, Thermoelectric properties of the 3C, 2H, 4H, and 6H polytypes of the wide-band-gap semiconductors SiC, GaN, and ZnO, *AIP Adv.*, 2015, **5**, 097204.

55 A. Janotti and C. G. Van de Walle, Native point defects in ZnO, *Phys. Rev. B: Condens. Matter Mater. Phys.*, 2007, **76**, 165202.

56 B. E. Sernelius, K.-F. Berggren, Z.-C. Jin, I. Hamberg and C. G. Granqvist, Band-gap tailoring of ZnO by means of heavy Al doping, *Phys. Rev. B: Condens. Matter Mater. Phys.*, 1988, **37**, 10244–10248.

57 A. Mang, K. Reimann and S. Rübenacke, Band gaps, crystal-field splitting, spin-orbit coupling, and exciton binding energies in ZnO under hydrostatic pressure, *Solid State Commun.*, 1995, **94**, 251–254.

58 H. Xiao, J. Tahir-Kheli and W. A. I. Goddard, Accurate Band Gaps for Semiconductors from Density Functional Theory, *J. Phys. Chem. Lett.*, 2011, **2**, 212–217.

59 P. Borlido, T. Aull, A. W. Huran, F. Tran, M. A. L. Marques and S. Botti, Large-Scale Benchmark of Exchange–Correlation Functionals for the Determination of Electronic Band Gaps of Solids, *J. Chem. Theory Comput.*, 2019, **15**, 5069–5079.

60 R. Wang and J.-C. Zheng, ZnO monolayer supported single atom catalysts for efficient electrocatalytic hydrogen evolution reaction, *Phys. Chem. Chem. Phys.*, 2024, **26**, 5848–5857.

61 S. S. Chong, Y. S. Ng, H.-Q. Wang and J.-C. Zheng, Advances of Machine Learning in Materials Science: Ideas and Techniques, *Front. Phys.*, 2024, **19**(1), 13501.